PCCP

PAPER

View Article Online
View Journal | View Issue

Cite this: *Phys. Chem. Chem. Phys.*, 2023, **25**, 6797

Oxygen diffusion in the orthorhombic $FeNbO_4$ material: a computational study†

Xingyu Wang, David Santos-Carballal and Nora H. de Leeuw *

ABO_4-type materials have shown significant potential for applications as luminescence and photocatalytic materials, and the orthorhombic $FeNbO_4$ (*o*-$FeNbO_4$) material has also shown excellent promise in catalytic electrodes, unlike other common ABO_4 materials. However, little computational work has been carried out on the *o*-$FeNbO_4$ structure, potentially because it is disordered and thus not straightforward to simulate. In this work, we first confirmed the accuracy of the force field parameters obtained from previous studies through optimizations carried out using the GULP code. Next, we found that one ordered configuration of the stoichiometric *o*-$FeNbO_4$ structure dominates when analysing the probabilities of cation disorder in three supercells ($2 \times 2 \times 1$, $2 \times 1 \times 2$, and $1 \times 2 \times 2$). We then studied the bulk properties of this selected *o*-$FeNbO_4$ through DFT calculations, including the lattice parameters, the mechanical properties and the electronic structures, where no remarkable differences were observed compared to the monoclinic $FeNbO_4$ structure. Finally, because oxygen mobility is key to the successful application of *o*-$FeNbO_4$ as an electrode material, we have simulated the diffusion pathways of oxygen through both the stoichiometric and non-stoichiometric structures, where the results show that the existence of oxygen vacancies enhances diffusion and the distribution of the Fe and Nb inside the lattice affects the energy barriers and could therefore impact the oxygen diffusion.

Received 5th September 2022,
Accepted 17th January 2023

DOI: 10.1039/d2cp04126j

rsc.li/pccp

1. Introduction

ABO_4-type oxides, *e.g.* $FeWO_4$, $FeVO_4$ or $LaTaO_4$, have shown significant promise as functional oxides in many applications, for example in super-capacitors and solar cell electrodes.[1–6] Generally, ABO_4 materials can be classified into two types on the basis of the valence of element B, *i.e.* +5 or +6. ABO_4 oxides with B = W^{6+} or Mo^{6+} have shown remarkable efficacy when used as super-capacitor and luminescence materials.[5,7,8] For example, it has been reported that green photoluminescence emission of $BaWO_4$ polymer nanohybrids was observed when the tetrahedral WO_4 structure was changed to the octahedral WO_6 structure,[7] and an intense blue photoluminescence emission could also occur in $BaWO_4$ powders due to the existence of defects around oxygen.[7,9] Other ABO_4-type materials (B = V^{5+}, Nb^{5+} and Ta^{5+}) normally show catalytic behaviour to some degree, as well as having potential as luminescence materials.[3,6,10] For example, $LaTaO_4$ doped with Eu is an interesting material for energy applications, as it catalyses aqueous methanol to generate hydrogen, whereas the $BiVO_4$/$FeVO_4$ heterojunction also displays similar photocatalytic performance when used to generate hydrogen through the splitting of water molecules.[2,10]

$FeNbO_4$, as a typical ABO_4 oxide, has shown good electrical and catalytic performance and thus has been developed for many years in applications such as gas sensing devices and solar energy conversion devices.[11–15] So far, three main $FeNbO_4$ structures have been observed during phase transitions, *i.e.* the monoclinic wolframite-type structure (*m*-$FeNbO_4$, space group $P2/c$), the orthorhombic α-PbO_2-type structure (*o*-$FeNbO_4$, space group *Pbcn*) and the rutile-type structure (*r*-$FeNbO_4$, space group $P42/mnm$). At temperatures below 1050 °C, *m*-$FeNbO_4$ is the most stable polymorph, where stable [FeO_6] and [NbO_6] octahedra are formed through coordinating one Fe^{3+} or Nb^{5+} with six oxygen ions.[16–18] Moreover, the Fe^{3+} and Nb^{5+} cations are distributed in an ordered fashion along zig-zag [FeO_6] and [NbO_6] octahedral chains.[16] Above 1050 °C, which is the temperature at which the cation distribution becomes disordered, a phase transition occurs from the monoclinic to orthorhombic structure which is completed near 1100 °C. The resulting material shows a typical α-PbO_2 structure, which remains stable in the temperature range from 1100–1380 °C. The second phase transition to generate the rutile-type structure is observed above 1380 °C and it remains stable until 1450 °C.[16,19] In recent years, both *m*- and *o*-$FeNbO_4$ materials have been explored for energy storage and conversion applications.[20–22] Interestingly, both *m*- and *o*-$FeNbO_4$ have shown potential as a replacement

School of Chemistry, University of Leeds, Leeds, LS2 9JT, UK.
E-mail: n.h.deleeuw@leeds.ac.uk

† Electronic supplementary information (ESI) available. See DOI: https://doi.org/10.1039/d2cp04126j

Table 1 Interatomic potential parameters used for the $FeNbO_4$

	Buckingham potential parameters		
Pairs	A (eV)	ρ (Å)	C (eV Å^6)
Fe^{3+}–$O_S^{-2.513}$	3219.34	0.2641	0
Fe^{2+}–$O_S^{-2.513}$	2763.94	0.2641	0
Nb^{5+}–$O_S^{-2.513}$	3023.18	0.3	0
$O_S^{-2.513}$–$O_S^{-2.513}$	25.41	0.6937	32.32
	Core–shell model parameters		
Ion	K_{cs} (eV Å^{-2})	q_{Oc} (e)	q_{Os} (e)
$O_C^{+0.513}$–$O_S^{-2.513}$	20.53	+0.513	−2.513

material for the Ni metal in the cathodes of solid oxide electrolysis cells (SOEC)[21,22] and the anodes of solid oxide fuel cells (SOFC),[20] where the splitting of water vapour takes place, although o-$FeNbO_4$ is more suitable in electrodes than m-$FeNbO_4$. It has been reported that, when m-$FeNbO_4$ is used as anode in SOFC, there is a clear weight loss during its operation,[20] caused by the ordering within the m-$FeNbO_4$ system, where Fe^{3+} and Nb^{5+} layers are distributed alternately through the structure. Fe^{3+} is unstable, especially when exposed to a hydrogen atmosphere when it is easy for the Fe^{3+} to be reduced to the Fe^{2+}, at the same time generating a water molecule, which causes the structure to collapse.[20] This does not occur in the disordered o-$FeNbO_4$ system and as such o-$FeNbO_4$ may be the more promising material in energy conversion applications.

In previous work,[23] we have employed calculations based on the density functional theory (DFT) to study the bulk and surface properties of m-$FeNbO_4$. Due to the disorder of the cations in the o-$FeNbO_4$ phase, it is more difficult to create a computational model to simulate its behaviours and properties, which is presumably the reason why few computational studies have been reported on the orthorhombic phase. In the present study, we have employed the SOD code[24] to construct all the inequivalent cation configurations within the o-$FeNbO_4$ structure to identify the most stable structures. In addition, we have investigated the existence of oxygen vacancies, which according to experimental results improve the electronic conductivity when introduced into the structure in small concentrations.[20–22,25] There are few experimental reports on the diffusion of oxygen within the material, and in this work, we have also employed DFT calculations to investigate oxygen diffusion pathways, which are important in providing the oxygen required for the reaction with hydrogen, when the materials is used in catalytic electrodes.[20–22]

2. Computational methods

2.1 Force field parameters

The General Utility Lattice Program (GULP) code[26,27] was employed to carry out calculations on a number of bulk properties. GULP is based on the Born model of ionic solids, which defines all atoms as charged spherical ions and describes their interactions through short-range repulsive and van der Waals forces and long-range Coulombic interactions.[28–30] The short-range interactions in this work are described through Buckingham potentials and we have applied the core–shell model for the polarizable oxygen ions, where the total charge of the oxygen anions is split between a massive core and a massless shell. The interatomic potential (IP) parameters to describe the interactions between the Fe–O, Nb–O and O–O pairs are applicable to the simulation of both the monoclinic and orthorhombic $FeNbO_4$ phases. The Fe–O_S, Nb–O_S and O_S–O_S potentials used in this work are those reported by Woodley and Bush[31,32] and are listed in Table 1. In addition, we have studied the effect of oxygen vacancies on the distribution of the cations in the orthorhombic phase, and to compensate the charges in the oxygen-vacant structures, we have assumed that the surplus electrons generated by the oxygen vacancy remain on the neighbouring iron ions, whose charge is reduced from Fe^{3+} to Fe^{2+}.

2.2 SOD calculations for the orthorhombic $FeNbO_4$

We have employed the Site Occupancy Disorder (SOD) code[24] to generate all of the Fe and Nb cation configurations within the orthorhombic $FeNbO_4$ structure. We have built $2 \times 2 \times 1$, $2 \times 1 \times 2$ and $1 \times 2 \times 2$ supercell models to obtain the energetically optimum mixed structures. All inequivalent configurations within the $2 \times 2 \times 1$, $2 \times 1 \times 2$ and $1 \times 2 \times 2$ models were transferred into the GULP code to calculate the free energies, which were then used in SOD to carry out the analysis of the probability distribution of the inequivalent configurations. We have also carried out the same process on non-stoichiometric $2 \times 2 \times 1$ models, to determine the dominant phases when oxygen vacancies are present in the structure.

2.3 DFT calculations

In this work, all the DFT calculations were carried out using the Vienna *Ab initio* Simulations Package, VASP (version 5.4.4),[33–36] where we obtained the bulk properties of the preferred o-$FeNbO_4$ model selected from the probabilities calculations above. The ion-electron interactions and the exchange–correlation interactions are described through the projector-augmented wave method (PAW)[37] and the generalized gradient approximation (GGA)[38] with the Perdew–Burke–Ernzerhof (PBE) density functional, respectively. Spin-polarization was employed in all calculations and we have treated the following as valence electrons: Fe ($3p^6 3d^7 4s^1$), Nb ($4p^6 5s^1 4d^4 4s^2$), O ($2s^2 2p^4$). In addition, to improve the description of the electronic structures, we have used the on-site Coulombic interaction (DFT+U)[39] for the Fe 3d electrons with the $U_{eff} = U - J$ value of 4.3 eV. Following test calculations, the kinetic energy cut-off for the plane wave basis was set at 500 eV and the Henkelman algorithm was used to calculate the Bader charges.[39] In addition, $3 \times 3 \times 3$ gamma centered Monkhorst Pack grids were used for the simulation of the $2 \times 2 \times 2$ bulk. We have considered the spin distribution of Fe atoms in the orthorhombic phase as a quasi-random one and this phase could be generated through the Alloy Theoretic Automated Toolkit (ATAT), which was employed in the special quasi-random structures (SQS) method.[40–43]

In the final part of the paper, we have simulated the diffusion of oxygen through the o-$FeNbO_4$ lattice, where we have first placed an extra oxygen atom into an interstitial site inside the lattice and moved this atom in different directions.

Table 2 Experimental and computational results for the monoclinic $FeNbO_4$ lattice cell. (The experimental data of 1 and 2 show *P*2/*a* symmetry, while the data of experiments 3 and 4 show *P*2/*c* symmetry; we have swapped the *a* and *c* parameters of experiments 1 and 2 to make it consistent with the others)

	Experiment 1[47]	Experiment 2[18]	Experiment 3[48]	Experiment 4[19]	DFT[23]	GULP
a	5.008	4.992	4.646	4.650	4.687	4.697
b	5.632	5.607	5.615	5.616	5.691	5.573
c	4.656	4.637	4.996	4.998	5.038	5.102
β	90.27	90.06	89.85	90.15	90.44	87.31
Fe (*y*)	0.6742	0.6687	0.6680	0.1713	0.1657	0.1528
Nb (*y*)	0.1807	0.1824	0.1811	0.6799	0.6813	0.6720
O1 (*x*)	0.9402	0.919	0.2270	0.2251	0.2311	0.2234
O1 (*y*)	0.138	0.116	0.1106	0.1187	0.1172	0.1021
O1 (*z*)	0.774	0.767	0.9227	0.9113	0.9161	0.9134
O2 (*x*)	0.425	0.418	0.2704	0.2981	0.2754	0.2684
O2 (*y*)	0.384	0.384	0.3812	0.3827	0.3853	0.3920
O2 (*z*)	0.725	0.738	0.4177	0.437	0.4228	0.4384

In order to obtain a good understanding of the diffusion pathways, we have employed the static lattice method, which has been used by Saadoune, Baykov and others,[44–46] to determine the possible pathways. In this method, the diffusing atoms are fixed along the pathway, with the other atoms allowed to optimise fully, thereby avoiding the formation of stable structures which are not part of the diffusion pathways. Compared to the climbing image nudged elastic band (CI-NEB) method, which aims to find the saddle point in chemical reactions, the energy of transition states obtained through the static lattice method may be underestimated but it is a good description, and comparison, of different possible diffusion pathways.

3. Results and discussion

3.1 The GULP results

Elucidating the most probable cation configurations in the orthorhombic phase through the SOD and GULP codes requires suitable IP parameters. To this end, we have first employed the listed force field parameters in the GULP code to optimize the ordered monoclinic phase, and by evaluating whether the computational results are close to the experimental data, we could demonstrate the capability of the IP parameters to describe the interatomic interactions and next use them to simulate the orthorhombic phase.

The lattice parameters of the monoclinic $FeNbO_4$ (*m*-$FeNbO_4$) structure after optimization are listed in Table 2 and compared with a number of experimental results. The four structures obtained from experiments have been plotted in Fig. S1, S2 (ESI†), and by comparing the structure of experiments 3 and 4, we found that exchanging the Fe position for Nb does not affect the octahedral arrangement and the structural properties. The difference between the structures of experiments 1, 2 and 3, 4 is that experiments 1 and 2 show *P*2/*a* symmetry, while the structures in experiments 3 and 4 have *P*2/*c* symmetry, in which the parameters *a* and *c* are swapped compared to experiments 1 and 2. The computational results from the DFT calculations, discussed in detail in our previous work,[23] are generally more accurate than those obtained from GULP, where all lattice parameters except for the *β* angle vary slightly from the DFT data. However, the error is within an acceptable margin and the force field parameters in Table 1 are accurate enough to employ in the rest of the work.

To further validate the IP parameters, we have optimised both the monoclinic and orthorhombic $FeNbO_4$ structures. The relaxed lattice energies and structural parameters are listed in Table 3. They show that the lattice energy of *m*-$FeNbO_4$ is lower than the *o*-$FeNbO_4$, which is consistent with experiment in that *m*-$FeNbO_4$ should be more stable than *o*-$FeNbO_4$.

Table 3 The lattice parameters and lattice energy of *m*-$FeNbO_4$ and *o*-$FeNbO_4$ from GULP simulations

	a (Å)	*b* (Å)	*c* (Å)	*β* (°)	Lattice energy
m-$FeNbO_4$	4.697	5.573	5.102	87.31	−481.795
o-$FeNbO_4$	4.679	5.526	5.096	90.00	−481.687

3.2 The dominant phase of the stoichiometric orthorhombic $FeNbO_4$

In the SOD code, the number of inequivalent cation configurations in a 2 × 2 × 2 supercell of the disordered *o*-$FeNbO_4$ material would reach $C_{32}^{16} = \frac{32!}{16! \times 16!}$, which is an unrealistic number of configurations to compute. Thus, to still do a comprehensive study of the ordering in the structure, we have generated 2 × 2 × 1, 2 × 1 × 2, and 1 × 2 × 2 supercells. From Table 4, we note that in each of these supercells the total number of inequivalent configurations is $C_{16}^{8} = \frac{16!}{8! \times 8!} =$ 12 870, which number is reduced after consideration of the symmetry, to 482, 448, and 474 for the three supercells,

Table 4 Inequivalent configurations for the orthorhombic $FeNbO_4$

Supercell	Cell numbers (111)	Composition	Total configurations (N)	Inequivalent configurations (M)
2 × 2 × 1	4	$Fe_8Nb_8O_{32}$	12870	482
2 × 1 × 2	4	$Fe_8Nb_8O_{32}$	12870	448
1 × 2 × 2	4	$Fe_8Nb_8O_{32}$	12870	474

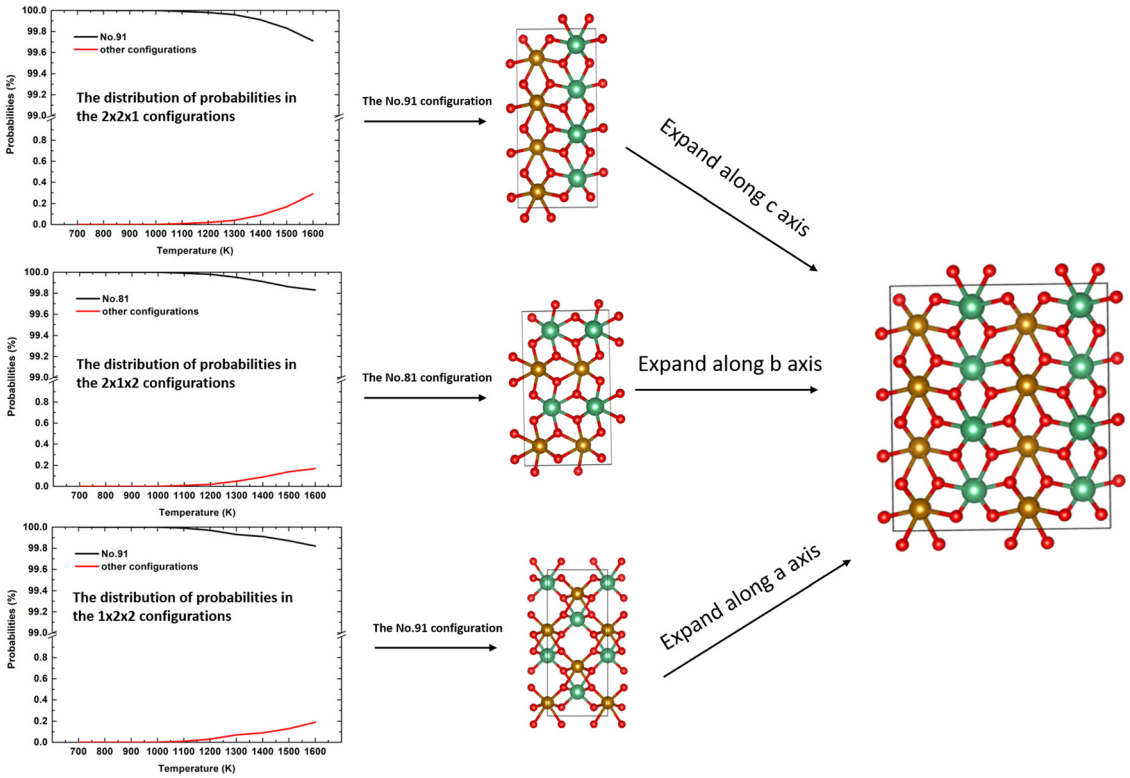

Fig. 1 The distributions of the probabilities in the 2 × 2 × 1, 2 × 1 × 2, and 1 × 2 × 2 supercells and the related most stable configurations; red is oxygen anion, brown is the Fe cation and green is the Nb cation.

respectively. The results of the calculations of the probability distributions are shown in Fig. 1 from which it is clear that from 700 K to 1600 K, there is one inequivalent configuration (labelled No. 91, No. 81 and No. 91) in each cell whose probability of occurrence exceeds 99.5%. If we expand each cell to a 2 × 2 × 2 supercell, we see that all 3 cells obtained the same dominant and ordered phase as the most probably configuration. As such, from our calculations, it appears that the most stable phase is an ordered structure rather than the disordered material observed experimentally. For the sake of completeness, we have also calculated the contributions of the vibrational entropy to the free energy of both structures, which are listed in Table S2 (ESI†). However, it is clear that the difference in entropy of the two phases is so small that we can ignore its contribution to the structural stabilities.

3.3 The lattice parameters, mechanical properties and electronic structures

Before optimising the structure, we have first confirmed the magnetic distribution inside the lattice (Fig. S3, ESI†) according to our former study and the work by Lakshminarasimhan and co-workers,[23,49] where the orthorhombic structure shows

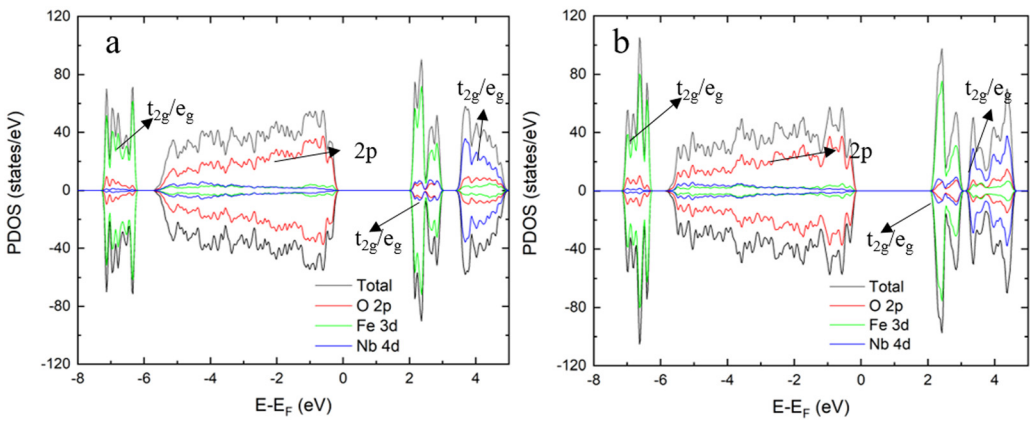

Fig. 2 The PDOS for the monoclinic $FeNbO_4$ (a) and the orthorhombic $FeNbO_4$ (b).

Table 5 The Bader charge, magnetic moment and bond distance of the *m*/*o*-$FeNbO_4$ lattices. Negative atomic magnetic moments indicate anti-parallel alignment

	o-$FeNbO_4$	*m*-$FeNbO_4$[23]
q_{Fe} (e)	+1.88	+1.89
q_{Nb} (e)	+2.72	+2.72
q_O (e)	−1.16/−1.31	−1.16/−1.30
μ_{Fe} (μ_B)	(±)4.17–(±)4.25	4.27
μ_{Nb} (μ_B)	0	0
μ_O (μ_B)	0	0
Fe–O distance (Å)	2.052	2.045
Nb–O distance (Å)	2.022	2.017

antiferromagnetic behaviour with small areas of spin glass. We next carried out DFT calculations to obtain a range of properties of the selected *o*-$FeNbO_4$, shown in Fig. 2 and Table 5. As a comparison, we have added the same data for the *m*-$FeNbO_4$ phase which show no remarkable differences in Bader charges or bond distances between the *o*-$FeNbO_4$ and *m*-$FeNbO_4$ structures. Interestingly, in the *o*-$FeNbO_4$ structure, the magnetic moment of Fe could not maintain the same value as in the *m*-$FeNbO_4$ structure, indicating that in a spin glass structure, the spin symmetry can be broken. In summary, both the results of the calculation of the probabilities and the electronic structure have demonstrated that the phase transition from the monoclinic to the orthorhombic structure does not impact the bulk properties.

We have also calculated the mechanical properties of the ordered *o*-$FeNbO_4$, including the elastic constants (C_{ij}), bulk modulus (B), shear modulus (G) and Young's modulus (E), again comparing with the *m*-$FeNbO_4$ material from our previous work.[23] We have employed VASP and the finite difference technique to obtain the values of the elastic constants C_{ij}, where the elastic tensor was obtained by performing finite distortions in the direction of each Cartesian coordinate of the lattice and deriving C_{ij} through the stress–strain method as:

$$C_{ij} = \frac{1}{V}\frac{\partial^2 E}{\partial\varepsilon_i \partial\varepsilon_j} \quad (1)$$

where E is the total energy of the stressed cell, V is the equilibrium volume and ε is the component of the applied strain. Having calculated the values of C_{ij}, we obtain the values of B, G, and E through the following equations:

$$B = \frac{[c_{11} + c_{22} + c_{33} + 2(c_{12} + c_{13} + c_{23})]}{9} \quad (2)$$

$$G = \frac{[c_{11} + c_{22} + c_{33} + 3(c_{44} + c_{55} + c_{66}) - (c_{12} + c_{13} + c_{23})]}{15} \quad (3)$$

$$E = \frac{9BG}{3B + G} \quad (4)$$

In contrast to the monoclinic phase, there are 9 independent elastic constants (C_{11}, C_{22}, C_{33}, C_{44}, C_{55}, C_{66}, C_{12}, C_{13}, and C_{23}) for the orthorhombic structure, all listed in Table 6. We found that the C_{11} of *m*-$FeNbO_4$ is smaller than that of *o*-$FeNbO_4$, while the converse is true for the C_{33}, indicating that along its *a* direction the *m*-$FeNbO_4$ phase is softer, while along the *c* direction it is harder than the *o*-$FeNbO_4$ phase. Next, we employed eqn (2)–(4) to calculate the values of the bulk modulus (B), the shear modulus (G) and the Young's modulus (E) and found that all moduli of the *m*-$FeNbO_4$ phase are a little larger than that of the *o*-$FeNbO_4$ phase, indicating the ability of the *o*-$FeNbO_4$ phase to resist compression and elastic shear strain but its tensile stiffness is not as good as that of the *m*-$FeNbO_4$ phase.

Table 6 The elastic constants and the mechanical properties of the *m*/*o*-$FeNbO_4$

Elastic constant (GPa)	*m*-$FeNbO_4$[23]	*o*-$FeNbO_4$
C_{11}	274.1	304.1
C_{22}	269.8	271.4
C_{33}	318.8	253.9
C_{44}	74.5	27.6
C_{55}	102.1	24.7
C_{66}	57.1	72.6
C_{12}	144.1	141.3
C_{13}	148.5	110.7
C_{23}	119.7	140.7
C_{15}	−6.8	—
C_{25}	−11.7	—
C_{35}	−22.9	—
C_{46}	10.2	—
B	187.5	179.4
G	76.8	54.1
E	202.7	147.5

Finally, we have compared the electronic structures of the *m*- and *o*-$FeNbO_4$, whose DOS plots are shown in Fig. 2. Generally, there is a very similar DOS distribution for the *m*/*o*-$FeNbO_4$ phases, except for a slight difference in the conduction band, where the integrated orbital is split into two small parts in the DOS of *o*-$FeNbO_4$ at around 4.0 eV. Both phases show typical semiconductor characteristic with a band gap between the conduction band maximum (CBM) and the valence band minimum (VBM), where the CBM is mainly comprised of the Fe 3d orbitals. Furthermore, it is believed that in the *m*-$FeNbO_4$ phase, the electron conduction mainly occurs in the FeO_6 layers along its *a* direction while after mixing the Fe and Nb, it is likely that the electron could be conducted through the 3D net inside.

3.4 Oxygen diffusion in the stoichiometric and non-stoichiometric structures

3.4.1 Oxygen diffusion through the stoichiometric *o*-$FeNbO_4$ structure. Next, we have introduced an extra interstitial oxygen atom into the 2 × 2 × 2 supercell, whose lattice is large enough that it does not affect the adjacent supercells, and used DFT to calculate the O diffusion pathways. In the stoichiometric *o*-$FeNbO_4$ structure shown in Fig. 3, the lowest energy location for the insertion of an extra oxygen into the lattice is the interstitial site shown in Fig. S4 (ESI†). The formation energy of the oxygen interstitial atom is relatively high at 2.2 eV and we would therefore not expect this defect to occur widely, but we have investigated this defect here for the sake of completeness. Once an interstitial oxygen atom has been inserted in the supercell, this oxygen atom could move to the adjacent interstitial site through pathways in the 3D networks. We have considered a number of plausible

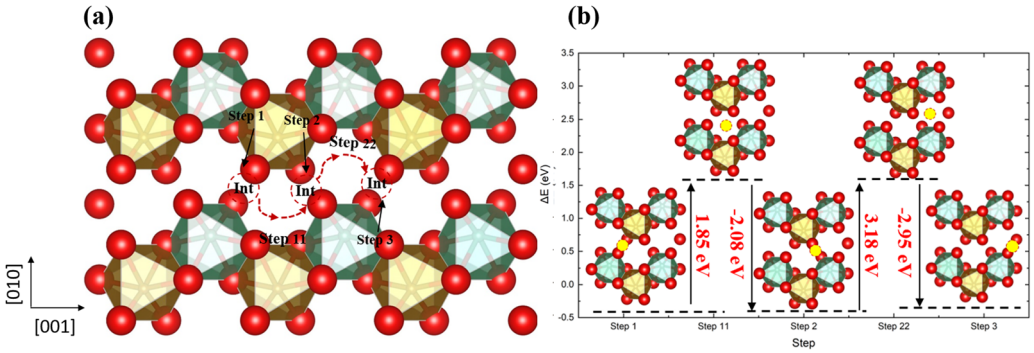

Fig. 3 The diffusion pathway of the interstitial oxygen atom along the [001] direction in the ordered stoichiometric structure (a), and the variation of the total energy (b); red is oxygen, brown is Fe, green is Nb and the yellow ball in (b) is the interstitial oxygen atom.

diffusion pathways, along the [100], [010], and [001] directions. The diffusion pathway along the [001] direction has been plotted in Fig. 3, whereas the other pathways are shown in our ESI† (Fig. S5 and S6). Along the [001] direction, shown in Fig. 3, the diffusion starts from the interstitial site, and then moves towards to the gap site, where an energy barrier (up to 3.18 eV) needs to be overcome to diffuse to the adjacent interstitial site. This behaviour is not unique to the [001] direction and can be seen in other pathways in Fig. S5 and S6 (ESI†).

In addition to the direct diffusion pathway, we have also studied the interstitialcy mechanism along the [001] direction, which is the dominant diffusion pathway in many metal oxides.[50,51] The result is plotted in Fig. 4, showing an initial energy barrier of 3.89 eV, *i.e.* considerably larger than in the direct diffusion pathway. This therefore suggests that in $FeNbO_4$ materials the direct diffusion pathway should dominate, owing to the energetic cost of moving a lattice oxygen to the interstitial site compared to it moving through a gap site.

3.4.2 Diffusion of oxygen through oxygen-deficient $FeNbO_4$. Next, we have introduced an oxygen vacancy into the *o*-$FeNbO_4$ phase to study the oxygen diffusion in the presence of oxygen vacancies, as can be expected to occur in experimental electrode materials, also using DFT. There are two sites for the oxygen vacancy in the simulation cell of the ordered material, *i.e.* labelled V_{O1} which is surrounded by one FeO_6 and two NbO_6 octahedral, and labelled V_{O2} which is surrounded by two FeO_6 and one NbO_6 octahedral, shown in Fig. 5. Before studying the diffusion of the oxygen in this non-stoichiometric phase, we have calculated the formation energies of both vacancy types, also shown in Fig. 5, according to the equation: $E_f = E_{defective} - E_{bulk} + \frac{1}{2}E_{O_2}$, where $E_{defective}$ and E_{bulk} are the total energies of the non-stoichiometric material and the stoichiometric bulk material, respectively, and E_{O_2} refers to the total energy of the oxygen molecule in the triplet ground state. The lattice parameters and lattice energies of the optimized structures are listed in Table S1 (ESI†), which show that the lattice with V_{O1} type vacancies is the most distorted structure in terms of volume and lattice energy. Overall, V_{O2} is the preferred oxygen vacancy site in the lattice due to its lower formation energy, although at 3.7 eV it is still a very high value, in agreement with experimental records which show that most oxygen vacancies are generated in the preparation process at temperatures of 1100 °C.[16–20] We have therefore introduced the V_{O2} in the 2 × 2 × 2 supercells to investigate the oxygen diffusion pathways, where we noted that the formation energy of the oxygen vacancies does not change as the supercell is increased in size, which indicates that the reduction is a localised process, also shown by the short-range lattice distortion around the vacancy sites.

Usually, the oxygen atom in the oxygen vacancy-containing oxide materials prefers to diffuse through a hopping mechanism, similar to the process reported in $BaFeO_3$, $SrCoO_3$, and CeO_2 materials.[52–55] Fig. 6 shows two possible pathways for this type of diffusion, where in Fig. 6a, the oxygen atom hopping occurs along the [001] direction with the nearest neighbouring

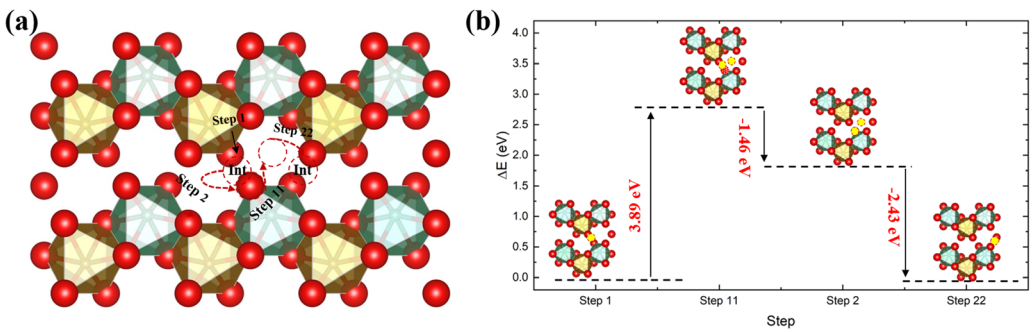

Fig. 4 The diffusion pathway of the interstitial mechanism along the [001] direction in the ordered stoichiometric structure (a), and the variation of the total energy (b); red is oxygen, brown is Fe, green is Nb and the yellow ball in (b) is the interstitial oxygen atom.

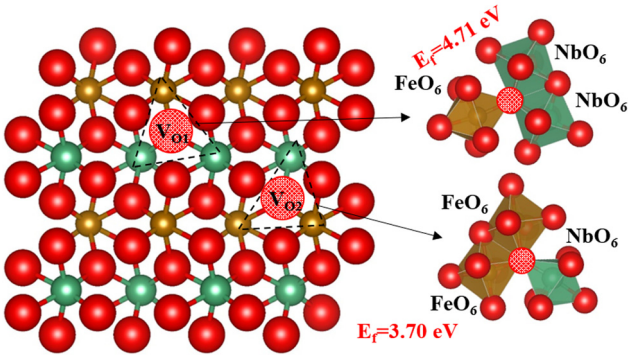

Fig. 5 The types of oxygen vacancies in the ordered *o*-$FeNbO_4$; oxygen is red, Fe is brown, Nb is green and the red ball with black pattern represents the oxygen vacancy.

oxygen hopping into the original and newly generated vacancy sites. The energy barriers are shown in Fig. 6b, where the vacancy sites 2 and 4 (type V_{O1}) are less stable than the other three (1, 3 and 5 which are type V_{O2} vacancies). Thus, from step 1 to 2, there is an energy barrier of ~1.04 eV, similar to the barrier from step 2 to 3 (~1.03 eV). Finally, when the vacancy is transferred to site 5 (V_{O2}) from 4 (V_{O1}), the structure is stabilised again.

Along the [110] direction (Fig. 6c), which can be seen as a combination of the diffusion pathways along [010] and [100], all the energy barriers have similar values (~0.2 eV), since all vacancies along this pathway are type V_{O2} vacancies. Therefore, although the oxygen could diffuse through the vacancy sites in the [100] way, the [110] pathway is energetically favourable. As expected, the presence of oxygen vacancies benefits oxygen diffusion through the lattice. In addition, we have noticed that for the oxygen atom, diffusing in the [110] direction is much easier than the [001] direction, since in the ordered structure all the vacancies along the [110] belong to the V_{O2} type.

3.4.3 The effect of cation disorder on the oxygen diffusion. Since experimentally the orthorhombic phase is found to be disordered, we can also expect configurations with different Nb and Fe cation distributions to exist within the material. It has been reported that oxygen vacancies are found in the orthorhombic $FeNbO_4$ structure, which will increase cation mobility and the likelihood of cation disorder in the lattice.[25,47,56] We have demonstrated that the formation energy of oxygen vacancies depends on the oxygen site, and our earlier results suggest that if an oxygen were to be surrounded by three FeO_6 octahedra, the formation energy of the oxygen vacancy will be reduced even further. To test this hypothesis using our DFT calculations, we have created a $2 \times 2 \times 1$ supercell with this type of oxygen site and created the oxygen vacancy V_{O3}, as shown in Fig. 7. As hypothesised, the oxygen formation energy at 2.82 eV is indeed lower than that for the former two oxygen vacancy types (3.70 eV and 4.71 eV for V_{O2} and V_{O1} respectively). Next, we have investigated this oxygen vacancy-containing configuration with SOD and GULP to simulate the probabilities of its inequivalent configurations. Note that for these simulations, we assigned the two electrons left behind by the O atoms to the two Fe cations closer to the O vacancy, which oxidation number was reduced to +2.

The probabilities of the non-stoichiometric structures containing oxygen vacancies are plotted in Fig. 8, where we observe four main structures from 700 K to 1600 K, in addition to the dominant structure, No. 7069, which is shown in Fig. 8b. These configurations are all different from the dominant ordered

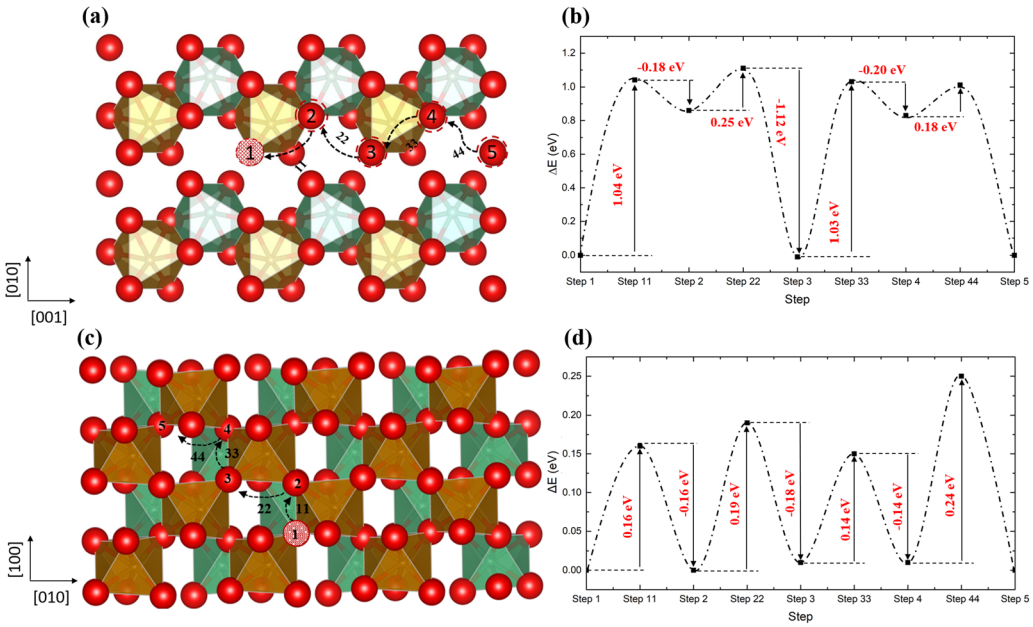

Fig. 6 The diffusion pathways of the oxygen atom along the [001] direction (a) and the [110] direction (c) in the ordered non-stoichiometric structures with an oxygen vacancy and their corresponding energy barriers (b and d); red is oxygen, brown is Fe, green is Nb and the red ball with black pattern represents the oxygen vacancy.

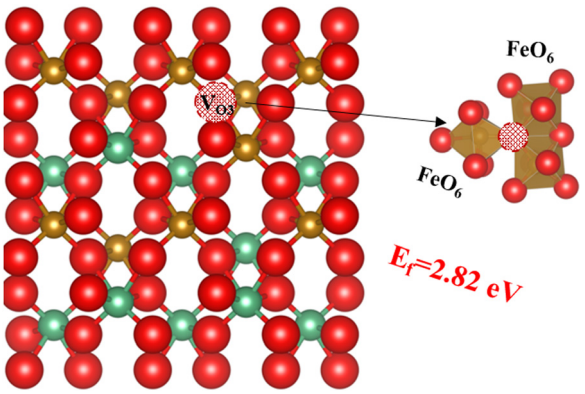

Fig. 7 The third type of oxygen vacancy; oxygen is red, Fe is brown, Nb is green and the red ball with black pattern represents the oxygen vacancy.

phase, discussed earlier, and our findings therefore suggest that when oxygen vacancies are present, cation disorder is more likely to occur, which could be the origin of the disordered materials found in experiment.

In order to gain insight into the impact of the cation distribution on the oxygen diffusion, we have employed the $2 \times 2 \times 2$ supercell in Fig. 8c, with different cation distributions along the diffusion pathways. In order to make the calculations tractable, we have selected pathways where the oxygen diffuses through a vacancy hopping mechanism. The same two pathways as identified in the ordered structure are plotted in Fig. 9. Along the [001] direction, the sequence of vacancy types is: V_{O3}(step1)–V_{O1}(step2)–V_{O2}(step3)–V_{O2}(step4)–V_{O3}(step5), in contrast to the ordered structured where V_{O1} and V_{O2} alternate. From step 1 to step 2, the energy barrier to be surmounted is

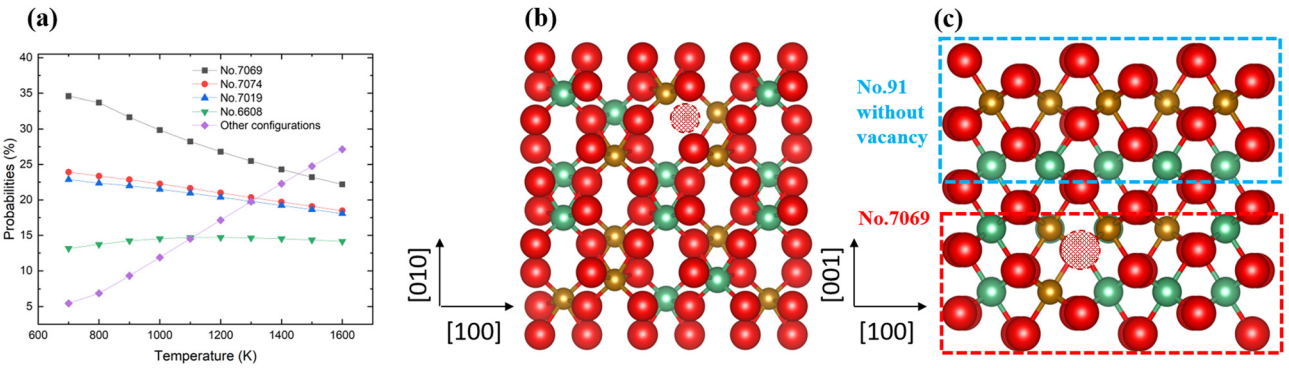

Fig. 8 The distributions of the probabilities in the defect $2 \times 2 \times 1$ supercell (a); the most stable No. 7069 configuration (b) and the $2 \times 2 \times 2$ supercell used in this work (c).

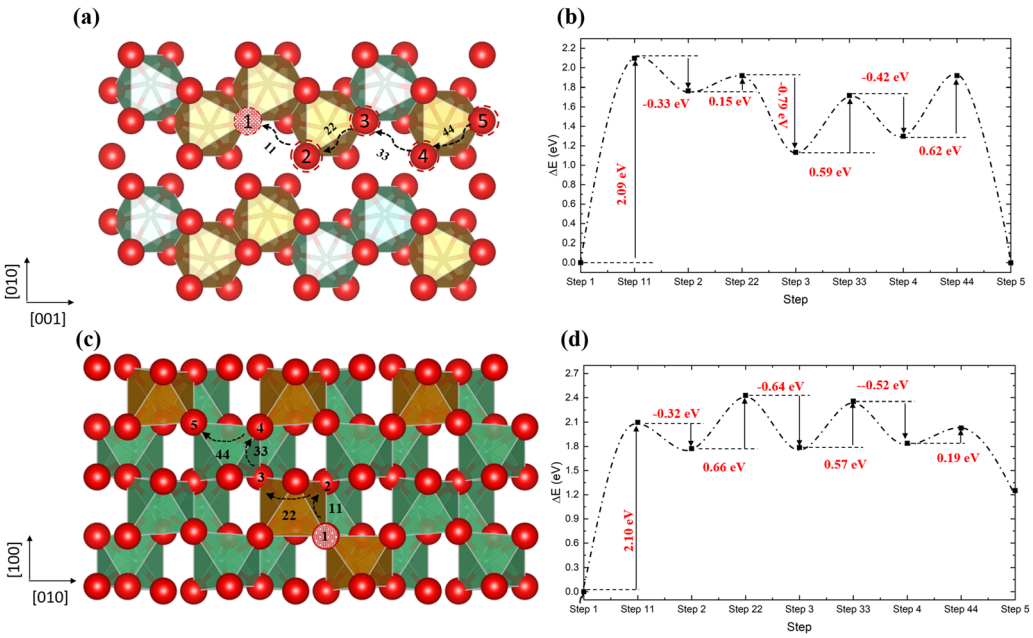

Fig. 9 The diffusion pathways of the oxygen atom along the [001] direction (a) and the [110] direction (c) in the disordered non-stoichiometric structures with an oxygen vacancy and their corresponding energy barriers (b and d); red is oxygen, brown is Fe, green is Nb and the red ball with black pattern represents the oxygen vacancy.

2.09 eV to create V_{O1}, where the total energy of the system is almost at its highest, before the vacancy hops to the more stable V_{O2} type, only having to overcome a very small further barrier of 0.15 eV. Next on the pathway, another V_{O2} is created, for which an energy barrier of 0.59 eV has to be overcome, followed by a similar barrier of 0.62 eV to finally form another V_{O3}. Similar results are found in the [110] direction, where in the first two steps, the vacancy moves from V_{O3} to V_{O1} with a barrier of 2.10 eV, but releasing 0.66 eV to form a V_{O1} site. When we compare these results with the diffusion in the ordered structure in Fig. 6, we note that in the disordered structure the initial energy barrier for the oxygen to move into the V_{O3} site at about 2.10 eV is much higher than in the ordered structure, owing to the stability of the V_{O3} vacancy, and oxygen diffusion through the disordered structure will therefore be slower.

4. Conclusion

In this work, we have created $2 \times 2 \times 1$, $1 \times 2 \times 2$ and $2 \times 1 \times 2$ supercells of the *o*-$FeNbO_4$ material to confirm the dominant cation configuration(s) within the *o*-$FeNbO_4$ structures, and we have studied the related bulk properties of the dominant *o*-$FeNbO_4$ phase by DFT calculations. For the stoichiometric material, the results all confirmed a single dominant, ordered configuration with a probability of occurrence that exceeds 99.5%, which was selected for more in-depth study. The bulk properties of this selected *o*-$FeNbO_4$ phase showed that there is no marked difference from the monoclinic $FeNbO_4$ phase, which was studied in previous work. We have also investigated the probabilities of cation disorder in the non-stoichiometric material containing an oxygen vacancy, where we identified a number of potential cation configurations. We therefore suggest that oxygen vacancies, which are present in experimental materials, may encourage the cation disorder in the orthorhombic $FeNbO_4$ phase observed experimentally.

We have simulated oxygen diffusion pathways in the ordered stoichiometric material and in the non-stoichiometric ordered and disordered structures. In the stoichiometric material, the diffusion of an interstitial oxygen atom could occur only by surmounting an energy barrier of around 3 eV, whereas in the non-stoichiometric ordered structure, it is much easier for the oxygen to diffuse in a vacancy hopping mechanism along the [110] direction (energy barrier up to $\sim$0.24 eV) than along the [001] direction (up to $\sim$1.04 eV), since in the [110] direction all the diffusion sites belong to the V_{O2} vacancy type, while in the [001] direction, some sites are of the energetically less favourable V_{O1} type. In addition, we found that the distribution of the cations in the structure could impact the energy barriers along the pathways. In particular, during the vacancy hopping mechanism, vacancies are more stable in sites which are coordinated by fewer Nb–O bonds and more Fe–O bonds. When a disordered structure contains the low-energy V_{O3} vacancy sites, the initial energy barrier for vacancy hopping is $\sim$2.10 eV, and oxygen diffusion through non-stoichiometric disordered structures should therefore be slower.

We consider that this work has contributed detailed atomic-level insight into the orthorhombic $FeNbO_4$ material, where our results suggest that intrinsic oxygen vacancies promote oxygen diffusion through the vacancy hopping mechanism, but cation disorder may slow oxygen diffusion by allowing more stable vacancy sites to be formed. These are therefore two parameters that could be the focus in experimental syntheses to improve the efficacy of *o*-$FeNbO_4$ as a cathode material in solid oxide fuel cells.

Conflicts of interest

There are no conflicts to declare.

Acknowledgements

Xingyu Wang acknowledges the China Scholarship Council (CSC) [No. 201906460008] and the University of Leeds for a PhD scholarship. This work has used the computational facilities of the Advanced Research Computing at Cardiff (ARCCA) Division, Cardiff University and HPC Wales, and the high performance computing facilities (ARC4) provided by the University of Leeds. We also acknowledge computing resources on the UK's national supercomputing service ARCHER2 facility (**http://www.archer2.ac.uk**) *via* our membership of the UK's HEC Materials Chemistry Consortium, which is funded by EPSRC (EP/L000202).

References

1 E. S. Kim, C. J. Jeon, P. G. Clem and A. Feteira, Effects of Crystal Structure on the Microwave Dielectric Properties of ABO_4 (A = ni,Mg,Zn and B = mo,W) Ceramics, *J. Am. Ceram. Soc.*, 2012, **95**, 2934–2938.

2 A. H. Krumpel, P. Boutinaud, E. van der Kolk and P. Dorenbos, Charge Transfer Transitions in the Transition Metal Oxides ABO_4:Ln^{3+} and ABO_4:Ln^{3+} (a = La, Gd, Y, Lu, Sc; B = V, Nb, Ta; Ln = Lanthanide), *J. Lumin.*, 2010, **130**, 1357–1365.

3 J. Li, W. Zhao, Y. Guo, Z. Wei, M. Han, H. He, S. Yang and C. Sun, Facile Synthesis and High Activity of Novel $BiVO_4$/$FeVO_4$ Heterojunction Photocatalyst for Degradation of Metronidazole, *Appl. Surf. Sci.*, 2015, **351**, 270–279.

4 Y. Tian, Y. Tian, P. Huang, L. Wang, Q. Shi and C. E. Cui, Effect of Yb^{3+} Concentration on Upconversion Luminescence and Temperature Sensing Behavior in Yb^{3+}/Er^{3+} Co-Doped $YnBO_4$ Nanoparticles Prepared Via Molten Salt Route, *Chem. Eng. J.*, 2016, **297**, 26–34.

5 Z. Gu and X. Zhang, Nico2o4@Mnmoo4 Core–Shell Flowers for High Performance Supercapacitors, *J. Mater. Chem. A*, 2016, **4**, 8249–8254.

6 M. Nyman, M. A. Rodriguez, L. E. S. Rohwer, J. E. Martin, M. Waller and F. E. Osterloh, Unique $LaTaO_4$ Polymorph for Multiple Energy Applications, *Chem. Mater.*, 2009, **21**, 4731–4737.

7 Y. Oaki and H. Imai, Room-Temperature Aqueous Synthesis of Highly Luminescent $BaWO_4$–Polymer Nanohybrids and Their Spontaneous Conversion to Hexagonal WO_3 Nanosheets, *Adv. Mater.*, 2006, **18**, 1807–1811.
8 V. B. Mikhailik, H. Kraus, V. Kapustyanyk, M. Panasyuk, Y. Prots, V. Tsybulskyi and L. Vasylechko, Structure, Luminescence and Scintillation Properties of the $MgWO_4$–$MgMoO_4$ system, *J. Phys.: Condens. Matter*, 2008, **20**, 365219.
9 G. Zhou, M. Lü, Z. Xiu, S. Wang, H. Zhang and W. Zou, Polymer Micelle-Assisted Fabrication of Hollow $BaWO_4$ Nanospheres, *J. Cryst. Growth*, 2005, **276**, 116–120.
10 J. Deng, J. Jiang, Y. Zhang, X. Lin, C. Du and Y. Xiong, $FeVO_4$ as a Highly Active Heterogeneous Fenton-Like Catalyst Towards the Degradation of Orange Ii, *Appl. Catal., B*, 2008, **84**, 468–473.
11 C. Balamurugan, A. R. Maheswari, D. W. Lee and A. Subramania, Selective Ethanol Gas Sensing Behavior of Mesoporous N-Type Semiconducting $FeNbO_4$ Nanopowder Obtained by Niobium–Citrate Process, *Curr. Appl. Phys.*, 2014, **14**, 439–446.
12 K. I. Gnanasekar, V. Jayaraman, E. Prabhu, T. Gnanasekaran and G. Periaswami, Electrical and Sensor Properties of $FeNbO_4$: A New Sensor Material, *Sens. Actuators, B*, 1999, **55**, 170–174.
13 S. Kanti Biswas, T. Gnanasekaran, T. Kumar Ghorai and P. Pramanika, Sensing Properties of Chemically Synthesized Pristine and Pt-Impregnated Nanosized $FeNbO_4$ in Hydrogen, Ammonia, and Lpg, *J. Electrochem. Soc.*, 2008, **155**, J26–J31.
14 S. H. Ahmed, M. Bakiro and A. Alzamly, Visible-Light-Driven Photocatalytic Formation of Propylene Carbonate Using $FeNbO_4$/Reduced Graphene Oxide Composites, *Materialia*, 2020, **12**, 100781.
15 N.-S. Cho, S. Lee, J. H. Noh, G. K. Choi, H. S. Jung, D. W. Kim and K. S. Hong, Visible-Light-Induced Photocatalytic Activity in Fenbo4 Nanoparticles, *J. Phys. Chem. C*, 2008, **112**, 18393–18398.
16 R. Theissmann, H. Ehrenberg, H. Weitzel and H. Fuess, Domain Structure and Lattice Strains in $FeNbO_4$, *Solid State Sci.*, 2005, **7**, 791–795.
17 S. Ananta, R. Brydson and N. W. Thomas, Synthesis, Formation and Characterisation of $FeNbO_4$ Powders, *J. Eur. Ceram. Soc.*, 1999, **19**, 489–496.
18 V. M. Harder and H. Muller-Buschbau, $FeNbO_4$: Untersuchungen an Einkristallen Rnit Wolf Ramit- Und $AiNbO_4$-Struktur, *Z. Anorg. Allg. Chem.*, 1979, **456**, 99–105.
19 R. Theissmann, H. Ehrenberg, H. Weitzel and H. Fuess, Nanostructured Cation Distribution in $FeNbO_4$:A Synchrotron Powder Diffraction and Transmission Electron Microscopy Investigation, *J. Mater. Sci.*, 2002, **37**, 4431–4436.
20 X. Liu, D. Xie, J. T. S. Irvine, J. Ni and C. Ni, An $FeNbO_4$-Based Oxide Anode for a Solid Oxide Fuel Cell (Sofc), *Electrochim. Acta*, 2020, **335**, 135692.
21 X. Liu, J. Zhou, D. Xie, J. Ni and C. Ni, $FeNbO_4$-Based Oxide Cathode for Steam Electrolysis, *Solid State Ionics*, 2020, **345**, 115181.
22 C. Ni, J. Feng, J. Cui, J. Zhou and J. Ni, Ann-Type Oxide $Fe_{0.5}Mg_{0.25}Ti_{0.25}Nb_{0.9}Mo_{0.1}O_{4-\Delta}$ for Both Cathode and Anode of a Solid Oxide Fuel Cell, *J. Electrochem. Soc.*, 2017, **164**, F283–F288.
23 X. Wang, D. Santos-Carballal and N. H. de Leeuw, Density Functional Theory Study of Monoclinic $FeNbO_4$: Bulk Properties and Water Dissociation at the (010), (011), (110), and (111) Surfaces, *J. Phys. Chem. C*, 2021, **125**, 27566–27577.
24 R. Grau-Crespo, S. Hamad, C. R. A. Catlow and N. H. de Leeuw, Symmetry-Adapted Configurational Modelling of Fractional Site Occupancy in Solids, *J. Phys.: Condens. Matter*, 2017, **19**, 256201.
25 L. Li, Y. Li, Y. Li, H. Ye, A. Lu, H. Ding, C. Wang, Q. Zhou, J. Shi and X. Ji, Influences of Fe Mn Ratio on the Photocatalytic Performance of Wolframite ($Fe_xMn_{1-X}WO_4$), *Chem. Geol.*, 2021, **575**, 120253.
26 J. D. Gale, Gulp: A Computer Program for the Symmetry-Adapted Simulation of Solids, *J. Chem. Soc., Faraday Trans.*, 1997, **93**, 629–637.
27 J. D. Gale and A. L. Rohl, The General Utility Lattice Program, *Mol. Simul.*, 2003, **29**, 291–341.
28 M. Born and J. E. Mayer, Zur Gittertheorie Der Ionenkristalle, *Phys. B*, 1932, **75**, 1–18.
29 J. E. Mayer, Dispersion and Polarizability and the van der Waals Potential in the Alkali Halides, *J. Chem. Phys.*, 1933, **1**, 270–299.
30 M. S. Islam, M. Cherry and C. R. A. Catlow, Oxygen Diffusion in $LaMnO_3$ and $LaCoO_3$ Perovskite-Type Oxides: A Molecular Dynamics Study, *J. Solid State Chem.*, 1996, **124**, 230–237.
31 T. S. Bush, J. D. Gale, C. R. A. Catlow and P. D. Battle, Self-Consistent Interatomic Potentials for the Simulation of Binary and Ternary Oxides, *J. Mater. Chem.*, 1994, **4**, 831–837.
32 S. M. Woodley, P. D. Battle, J. D. Gale and C. R. A. Catlow, The Prediction of Inorganic Crystal Structures Using a Genetic Algorithm and Energy Minimisation, *Phys. Chem. Chem. Phys.*, 1999, **1**, 2535–2542.
33 G. Kresse and J. Furthmiiller, Efficiency of Ab-Initio Total Energy Calculations for Metals and Semiconductors Using a Plane-Wave Basis Set, *Comput. Mater. Sci.*, 1996, **6**, 15–20.
34 G. Kresse and J. Furthmuller, Efficient Iterative Schemes for Ab Initio Total-Energy Calculations Using a Plane-Wave Basis Set, *Phys. Rev. B: Condens. Matter Mater. Phys.*, 1996, **54**, 11169–11186.
35 G. Kresse and J. Hafner, Ab Initio Molecular Dynamics for Open-Shell Transition Metals, *Phys. Rev. B: Condens. Matter Mater. Phys.*, 1993, **48**, 13115–13118.
36 G. Kresse and J. Hafner, Norm-Conserving and Ultrasoft Pseudopotentials for First-Row and Transition Elements, *J. Phys.: Condens. Matter*, 1994, **6**, 8245–8260.
37 P. E. Blochl, Projector Augmented-Wave Method, *Phys. Rev. B: Condens. Matter Mater. Phys.*, 1994, **50**, 17953–17979.
38 J. P. Perdew, K. Burke and M. Ernzerhof, Generalized Gradient Approximation Made Simple, *Phys. Rev. Lett.*, 1996, **77**, 3865–3868.
39 S. L. Dudarev, G. A. Botton, S. Y. Savrasov, C. J. Humphreys and A. P. Sutton, Electron-Energy-Loss Spectra and the

Structural Stability of Nickel Oxide: An Lsda+u Study, *Phys. Rev. B: Condens. Matter Mater. Phys.*, 1998, **57**, 1505–1509.

40 K. Jun, J. U. Lee, M. H. Chang and T. Oda, A Comparative Study on Modeling of the Ferromagnetic and Paramagnetic States of Uranium Hydride Using a DFT+U Method, *Phys. Chem. Chem. Phys.*, 2019, **21**, 17628–17639.

41 A. van de Walle, Multicomponent Multisublattice Alloys, Nonconfigurational Entropy and Other Additions to the Alloy Theoretic Automated Toolkit, *CALPHAD: Comput. Coupling Phase Diagrams Thermochem.*, 2009, **33**, 266–278.

42 A. van de Walle, M. Asta and G. Ceder, The Alloy Theoretic Automated Toolkit: A User Guide, *CALPHAD: Comput. Coupling Phase Diagrams Thermochem.*, 2002, **26**, 539–553.

43 A. van de Walle, P. Tiwary, M. de Jong, D. L. Olmsted, M. Asta, A. Dick, D. Shin, Y. Wang, L. Q. Chen and Z. K. Liu, Efficient Stochastic Generation of Special Quasirandom Structures, *CALPHAD: Comput. Coupling Phase Diagrams Thermochem.*, 2013, **42**, 13–18.

44 I. Saadoune, J. A. Purton and N. H. de Leeuw, He Incorporation and Diffusion Pathways in Pure and Defective Zircon $ZrSiO_4$: A Density Functional Theory Study, *Chem. Geol.*, 2009, **258**, 182–196.

45 M. Lontsi-Fomena, A. Villesuzanne, J. P. Doumerc, C. Frayret and M. Pouchard, A Density Functional Theory Study of Oxygen Diffusion in $LaAlO_3$ and $SrTiO_3$, *Comput. Mater. Sci.*, 2008, **44**, 53–60.

46 V. I. Baykov, P. A. Korzhavyi and B. Johansson, Diffusion of Interstitial Mn in the Dilute Magnetic Semiconductor (Ga,Mn)As: The Effect of a Charge State, *Phys. Rev. Lett.*, 2008, **101**, 177204.

47 E. Schmidbauer, Electrical Resistivity, Thermopower, and Fe Mössbauer Study of $FeNbO_4$, *J. Solid State Chem.*, 1997, **134**, 253–264.

48 H. Ehrenberg, G. Wltschek, R. Theissman, H. Weitzel, H. Fuess and F. Trouw, The Magnetic Structure of Fenbo4, *J. Magn. Magn. Mater.*, 2000, **218**, 261–265.

49 N. Lakshminarasimhan, A. K. N. Kumar, S. S. Chandrasekaran and P. Murugan, Structure-Magnetic Property Relations in $FeNbO_4$ Polymorphs: A Spin Glass Perspective, *Prog. Solid State Chem.*, 2019, **54**, 20–30.

50 J. Xu, J. Wang, A. Rakhmatullin, S. Ory, A. J. Fernández-Carrión, H. Yi, X. Kuang and M. Allix, Interstitial Oxide Ion Migration Mechanism in Aluminate Melilite $La_{1+X}Ca_{1-X}Al_3O_{7+0.5x}$ Ceramics Synthesized by Glass Crystallization, *ACS Appl. Energy Mater.*, 2019, **2**, 2878–2888.

51 M. Youssef and B. Yildiz, Predicting Self-Diffusion in Metal Oxides from First Principles: The Case of Oxygen in Tetragonal ZrO_2, *Phys. Rev. B: Condens. Matter Mater. Phys.*, 2014, **89**, 024105.

52 C. Chen, Z. M. Baiyee and F. Ciucci, Unraveling the Effect of La a-Site Substitution on Oxygen Ion Diffusion and Oxygen Catalysis in Perovskite $BaFeO_3$ by Data-Mining Molecular Dynamics and Density Functional Theory, *Phys. Chem. Chem. Phys.*, 2015, **17**, 24011–24019.

53 J. Koettgen, T. Zacherle, S. Grieshammer and M. Martin, Ab Initio Calculation of the Attempt Frequency of Oxygen Diffusion in Pure and Samarium Doped Ceria, *Phys. Chem. Chem. Phys.*, 2017, **19**, 9957–9973.

54 A. Kushima, D. Parfitt, A. Chroneos, B. Yildiz, J. A. Kilner and R. W. Grimes, Interstitialcy Diffusion of Oxygen in Tetragonal $La_2CoO_{4+\Delta}$, *Phys. Chem. Chem. Phys.*, 2011, **13**, 2242–2249.

55 C. Mitra, T. Meyer, H. N. Lee and F. A. Reboredo, Oxygen Diffusion Pathways in Brownmillerite $SrCoO_{2.5}$: Influence of Structure and Chemical Potential, *J. Chem. Phys.*, 2014, **141**, 084710.

56 B. Balzer and H. Langbei, Solid Solutions in the $FeNbO_4$-TiO_2 System, *Cryst. Res. Technol.*, 1996, **31**, 93–98.